Sequential self-propelled morphology transitions of nanoscale condensates enable a cascade jumping-droplet condensation

Shan Gao [a,c,1], Jian Qu [a,1], Zhichun Liu [b,*], Weigang Ma [c,*]

[a] School of Energy and Power Engineering, Jiangsu University, Zhenjiang 212013, China
[b] School of Energy and Power Engineering, Huazhong University of Science and Technology, Wuhan 430074, China
[c] Key Laboratory for Thermal Science and Power Engineering of Ministry of Education, Department of Engineering Mechanics, Tsinghua University, Beijing 100084, China

A B S T R A C T

Jumping-droplet condensation, namely the out-of-plane jumping of condensed droplets upon coalescence, has been a promising technical innovation in the fields of energy harvesting, droplet manipulation, thermal management, *etc.*, yet is limited owing to the challenge of enabling a sustainable and programmable control. Here, we characterized the morphological evolutions and dynamic behaviors of nanoscale condensates on different nanopillar surfaces, and found that there exists an unrevealed domino effect throughout the entire droplet lifecycle and the coalescence is not the only mechanism to access the droplet jumping. The vapor nucleation preferentially occurs in structure intervals, thus the formed liquid embryos incubate and grow in a spatially confined mode, which stores an excess surface energy and simultaneously provides a asymmetric Laplace pressure, stimulating the trapped droplets to undergo a dewetting transition or even a self-jumping, which can be facilitated by the tall and dense nanostructures. Subsequently, the adjacent droplets merge mutually and further trigger more multifarious self-propelled behaviors that are affected by underlying surface nanostructure, including dewetting transition, coalescence-induced jumping and jumping relay. Moreover, an improved energy-based model was developed by considering both the surface structure properties and the nano-physical effects, the theoretical prediction not only extends the coalescence-induced jumping to the nanometer-sized droplets but also correlates the surface nanostructure topology to the jumping velocity. Such a domino effect of nucleation-growth-coalescence on the ultimate morphology of droplet may offer a new strategy for designing functional nanostructured surfaces that serve to orientationally manipulate, transport and collect droplets, and motivate surface engineers to realize a stable cascade jumping-droplet condensation and achieve its performance ceiling.

1. Introduction

Vapor condensation, as a ubiquitous energy transfer process in nature, has been widely exploited in many industrial contexts, from the energy management [1] to water-energy nexus [2], seawater desalination [3] and power generation [4]. For nearly a century, the pursuit of an energy-efficient condensation never seems to cease [5]. It is well known that dropwise condensation, where the condensate forms discrete droplets, exhibits a heat transfer coefficient that is 4–7 times higher than filmwise condensation [6], due to the considerable thermal resistance of a continuous liquid film adhered to substrate. For dropwise condensation on a smooth hydrophobic surface, heat and mass transfer rely on the

condensate removal effect, and droplets are passively shed under gravitational force, whose critical departure size D_c is constrained to the capillary length, $D_c \sim 1$ mm for water [7]. Promisingly, the recent development of micro/nanostructured superhydrophobic surfaces has paved a new pathway to further diminish the droplet-surface affinity [8–10]. Especially in the past decade, a novel mode derived from the conventional gravity-driven dropwise condensation was discovered, where the merged microdroplets could spontaneously jump away from surfaces without any external assistance [11].

Termed "jumping-droplet condensation" enables a reduction in the departing droplet size by several orders of magnitude, and thus has been confirmed to further enhance heat transfer by up to 100% [12,13].

Attracted by its great potential for self-cleaning [14,15], anti-icing [16, 17], energy harvesting [18] and electronics cooling [19,20], many follow-up studies have explored the hydrodynamics and energetics of this self-propelled jumping behavior [21–26]. However, there is no consensus on how small a coalesced droplet can detach from a surface [27–32], which is associated with the Ohnesorge number $Oh = \mu/\sqrt{\rho\sigma R}$ that characterizing the relative importance of viscous *versus* capillary-inertial effects, where μ, ρ, σ and R are the liquid dynamics viscosity, the liquid density, the surface tension and the radius of droplet, respectively. While earlier researches once suggested that jumping events will not occur below a critical size of $D_c \sim 10$ μm (in large Oh range) [11,27,33], the minimum jumping-droplet radius R_c has exceeded the submicron scale in recent experimental observations [28], even some numerical evidences indicate that nanoscale coalescence-induced jumping should be possible [31,34–37]. It was revealed that R_c is also dependent on the surface topology and the finer structure would enable smaller jumping droplets [30], so some intriguing questions arise accordingly, how to predict the critical departure size by considering Ohnesorge number and surface structure properties comprehensively and whether the self-removal can be achieved for the naturally grown (condensed) nanodroplets?

Unfortunately, to date, the above issues have not been exactly solved despite many efforts to investigate the nanometric jumping droplets [31, 37–39] by molecular dynamics (MD) simulations. In previous studies, the nanodroplets were constructed artificially and placed on a certain location of surface, usually atop the surface structure, then these suspended Cassie droplets were forced to gather together and trigger the coalescence event, which will introduce undesired external disturbances and affect the coalescence hydrodynamics. Such a simulation setting is inconsistent with the actual condensation situations, where the naturally formed droplets with different wetting states and sizes merge with each other actively. Therefore, to directly and definitely confirm the existence of nanometric jumping-droplet condensation and probe the jumping characteristics of naturally condensed nanodroplets, it necessitates a more realistic MD simulation on the condensation involving the entire droplet lifecycle, *i.e.*, nucleation, growth, coalescence and departure.

From an energetic standpoint, the surface energy released upon coalescence ΔE_S is partially converted into the kinetic energy of droplet E_k after overcoming the adhesion work E_{adh} and the viscous dissipation E_{vis} [40,41]. It has been established that viscous effects dominate the coalescence process and suppress the jumping as the droplet size decreases (as Oh increases toward unity), so there is a theoretical critical jumping-droplet radius R_c and a cut-off Ohnesorge number Oh_c. However, the existing models generally simplified the underlying surface as smooth to predict the scaled jumping velocity U_j^* of micrometer-sized droplets ($U_j^* = U_j/U_{ci}$, where $U_{ci} = \sqrt{\sigma/\rho R}$ is the capillary-inertial velocity) [24,33,42,43], which is uncorrelated with the surface structure topography and little is known about the coalescence dynamics and energetics at a smaller length scale [32]. In addition, the prediction from continuum physics becomes far from certain with decreasing system size because of the inescapable nano-physical effects [44,45]. To sum up, it may not be appropriate to judge the coalescence-induced jumping only by the Ohnesorge number (liquid properties), the surface structure properties and the prominent factors at the nanoscale should also be considered comprehensively, so as to rationally extend the prediction of the surface-dependent jumping velocity to the nanoscale size and provide a more accurate energy analysis.

In this study, we characterized the morphology evolutions and dynamic behaviors of nanoscale condensates over the entire lifecycle and elucidate many intriguing phenomena that are neglected in experimental observations, through nonequilibrium molecular dynamics simulation and energy-based theory analysis. It is found that the condensed droplets sequentially possess various morphologies and self-propelled transitions in nucleation, growth and coalescence stages,

which not only actuate the droplet migration and jumping, but also show a cascade effect on the ultimate wetting state of droplet. Furthermore, we clarified that the spontaneous removal is also possible for the condensed nanodroplets and the jumping-droplet condensation is not actually a unitary pattern only dominated by the coalescence mechanism. These findings can provide a theoretical foundation to rationally design nanostructure surfaces for self-cleaning, droplet manipulation and water collection.

2. Simulation methods

To delve deeper into the morphological evolutions of nanoscale condensates during condensation, particularly the incipient behaviors of nucleating embryos, large-scale MD simulations were conducted as depicted in Fig. 1. In the model system with the dimensions of 54.3 nm × 54.3 nm × 54.3 nm, the nanopillar surfaces with various topologies and wettability were initially submerged in the saturated water vapor, and the bottom substrate is divided into the fixed layer, the phantom layer and the conduction layer [46]. The nanostructured surfaces consist of a square pillar array with width $W = 3.1$ nm, different height H, interpillar spacing S and intrinsic contact angle θ_0, and the surface solid fraction $\varphi_s = W^2/(W+S)^2$, roughness factor $f = 1 + 4WH/(S+W)^2$. For convenience, all geometric dimensions are normalized by W, and the dimensionless parameters are presented with an asterisk, *e.g.*, $S^* = S/W$, $H^* = H/W$. There are a total of 120 surfaces combined by these geometric and wettability parameters, as listed in Table 1.

To provide a stable temperature and pressure control in the saturated state, as shown in Figs. S1 and S2 of Supporting Information (SI), the top quarter of vapor domain was set as a vapor/heat source to continuously supply the saturated vapor, through the GCMD method that is a combination of the grand canonical Monte Carlo (GCMC) and the MD simulation [47,48].

To reduce the computational cost, the simpler copper atoms (Cu) were chosen to construct the solid surface with tunable wettability, and a coarse-grained (CG) model [49], where each CG water bead (W) represents four water molecules, was adopted to constitute the vapor based on the saturation density at a given temperature. The interactions of Cu-Cu and Cu-W were respectively described by the embedded atom model (EAM) potential and the 12–6 Lennard-Jones (LJ) potential, the forcefields parameters are listed in Table S2 of SI [50]. Morse potential was employed to describe the water properties exactly, the density,
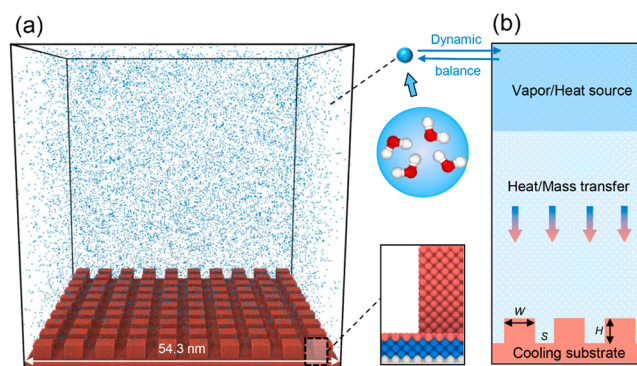
Fig. 1. (a) Initial configuration of the large-scale MD condensation model with a side-length of 54.3 nm. The bottom substrate is divided into the fixed layer, the phantom layer and the conduction layer, and the saturated vapor consists of the 4-site coarse-grained water beads. (b) Schematic illustration of the simulation domain settings. The top quarter region is used to replenish the vapor and heat by GCMD methods, and the water beads from the high-temperature vapor phase move to the cooling substrate and condense continuously, coupling with heat and mass transfer. The geometric parameters W, S and H denote the width, spacing and height of nanopillars, respectively.

Table 1
Geometric parameters ($W = 3.1$ nm, $S^* = S/W$, $H^* = H/W$) and wettability (intrinsic contact angle θ_0) for various nanopillar surfaces.

S^*	H^*	θ_0 (°)
0.5	0.25	126.47 ± 0.68
0.875	1	123.10 ± 0.45
1.25	1.75	117.06 ± 0.96
1.625	2.5	112.93 ± 0.61
2	—	106.97 ± 1.16
2.375	—	—

self-diffusion coefficient, heat of vaporization, free energy of solvation, surface tension and isothermal compressibility at 298 K were calculated to be 0.998 g/cm^3, 4.3×10^{-9} m^2/s, 38.4 kJ/mol, -28 kJ/mol, 0.071 N/m and 1.7×10^{-4} bar^{-1}, respectively. To quantitatively evaluate the wetting capacities of these solid surfaces, we calculated the intrinsic contact angles θ_0 of sessile cylindrical nanodroplets, eliminating the size-dependent deviation caused by line tension (see section S2 in SI for details) [51,52].

All these simulations involve two stages and were performed in LAMMPS software package [53]. To develop a steady solid-vapor coexistence at a temperature of 500 K, the entire system was first pre-equilibrated in a canonical (NVT) ensemble with the Nose-Hoover method for 1 ns. Then in the main simulation stage of 10 ns, the upper GCMD region was switched to a grand canonical (μVT) ensemble, while the remaining parts were integrated in a microcanonical (NVE) ensemble with a Langevin thermostat controlling the temperature of substrate (phantom layer) maintains at 300 K (see section S1 in SI for more simulation details).

3. Results

Based on the simulation results, the dynamic evolutions of condensed droplets were analyzed and discussed in the order of droplet lifecycle, and the condensed droplets forming on each surface were observed to range from ~ 1 nm to ~20 nm under our simulation conditions.
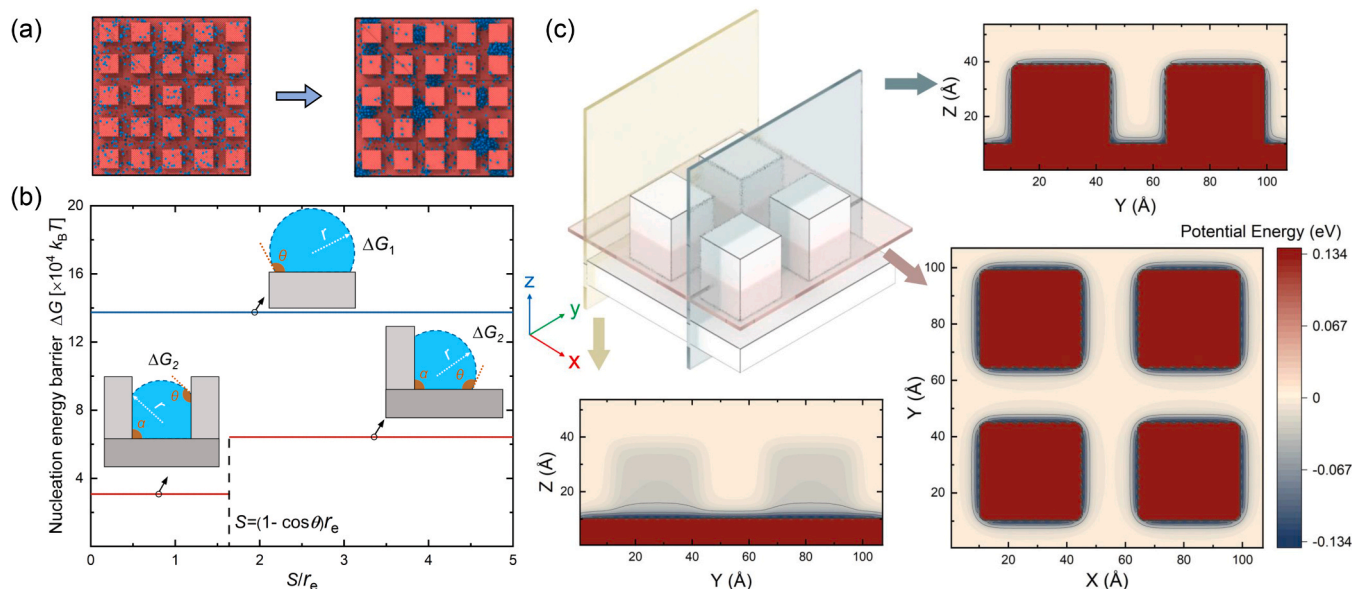
3.1. Preferential nucleation

In general, vapor condensation originates from the formation of liquid nuclei. To probe the nucleation characteristics, the nucleating embryos at the substrate-vapor interface were visualized. As shown in Fig. 2a, accompanied by the collisions with low-temperature surface, initially dispersed vapor beads were gradually captured and aggregated into clusters, *i.e.*, the condensing nuclei. Significantly, most nuclei regularly distributed within the surface roughness rather than atop the structure, showing a spatial preference of nucleation sites (see Video S1 of SI). This suggests that, for a homogeneous surface, liquid embryos nucleate in the crevices inevitably and the resultant droplets ought to immerse the surface if current trend continues, however, it is obviously inconsistent with the diverse wetting states (*e.g.*, suspended Cassie, immersed Wenzel and partial wetting) as observed in reality. We therefore infer that the ultimate morphology of a condensed droplet may be determined collaboratively by each stage of the droplet lifetime, and these cumulative effects will be further discussed in subsequent sections.

To understand the mechanism of preferential nucleation, the Gibbs free energy barrier of nucleation was analyzed according to the classical nucleation theory (CNT) [54]. For heterogeneous nucleation, provided that the radius of a liquid embryo is the critical nucleus size r_e, then its nucleation energy barrier ΔG can be expressed as [55,56].

$$\Delta G = -\frac{\rho V}{M} k_B N_A T_s \bullet \ln s + \sigma_{LV}(A_{LV} - A_{SL} \bullet \cos\theta) \qquad (1)$$

where ρ, V and M are the liquid density, the volume of embryo and the molar mass of liquid. k_B, N_A and T_s represent the Boltzmann constant, the Avogadro number and the surface temperature. s is the supersaturation defined as the ratio of vapor pressure P_∞ to the saturated vapor pressure P_s at T_s. σ_{LV}, A_{LV}, A_{SL} and θ represent the surface tension of liquid, the liquid-vapor interfacial area, the solid-liquid interfacial area and the Young's contact angle. Obviously, ΔG is directly connected with the nucleus shape that affected by the surface topology features, under a given thermodynamics condition. There are two typical nucleation configurations for the pillared surface studied here, namely the spherical-cap nucleus on the pillar top and the spherical-wedge nucleus at the pillar base, whose nucleation energy barriers ΔG_1 and ΔG_2 were calculated based on the above CNT model, as illustrated in Fig. 2b (calculation details of the nucleation energy barrier refer to the Section

Fig. 2. (a) Snapshots of the heterogeneous nucleation for water. (b) Nucleation energy barriers at different positions of the unit cell of nanopillar array. (c) Potential energy distributions of a CG water bead at a horizonal (XY-plane) cross section and two different vertical (YZ-plane) cross sections of the unit cell (2×2) of nanopillar array.

S3 in SI). The liquid-vapor boundary of nuclei embedded in the cavity is smaller than that atop the structure, and the reduced interfacial free energy lowers the energy barrier to overcome ($\Delta G_2 < \Delta G_1$). Hence, nucleation is more readily to occur in structure intervals. Moreover, ΔG_2 is also affected by the structure dimensions. As illustrated in the insets of Fig. 2b, given that the curvature radius of a nucleation droplet is equal to the critical nucleus size r_e, the droplet only contacts with a single pillar when the spacing S is large enough, but becomes sandwiched between the sidewalls of two pillars as S shrinks to a critical value $(1 - \cos\theta)r_e$ (see section S3 in SI), so ΔG_2 is further lowered in this situation, due to the reduction of liquid-vapor interfacial area.

Furthermore, to corroborate the preferential interface nucleation from a molecular-level view, we analyzed the potential energy distribution characteristics of the water bead at the solid-liquid interface. As displayed in Fig. 2c, a unit cell of roughness (four nanopillars) was chosen to calculate the potential energy U between one single water CG bead and all solid atoms based on the 12–6 LJ potential function. After obtaining the values of U in various positions, an horizontal (XY-plane) cross section and two different vertical (YZ-plane) cross sections were

selected to plot the potential energy contours, where there exists a distinct spatial nonuniformity that can affect vapor nucleation behaviors, and the low-potential-energy regions (nanostructure bases) approximately match with the initial nucleation sites. In these regions, the potent solid-liquid interactions promote the exchange of thermal energy, and meanwhile, the water beads are restricted more strongly. As a result, the vapor is inclined to nucleate nearby the nanostructure base, and the generated liquid embryos further incubate the condensate nanodroplets within a single unit cell of roughness (nanostructure valley), exhibiting a spatially preferential nucleation.

3.2. Spatially confined growth

After preferentially nucleating within structures, the liquid nuclei grow inside the unit cell of nanopillars continuously, and there emerged three representative modes classified by the dynamic behaviors of the generated nanodroplets (see Video S2 in SI, the corresponding pillar properties of each case are listed in Table S3 in SI). As shown in Fig. 3a, in the incipient growth stage, every nucleated droplet exhibits a roughly
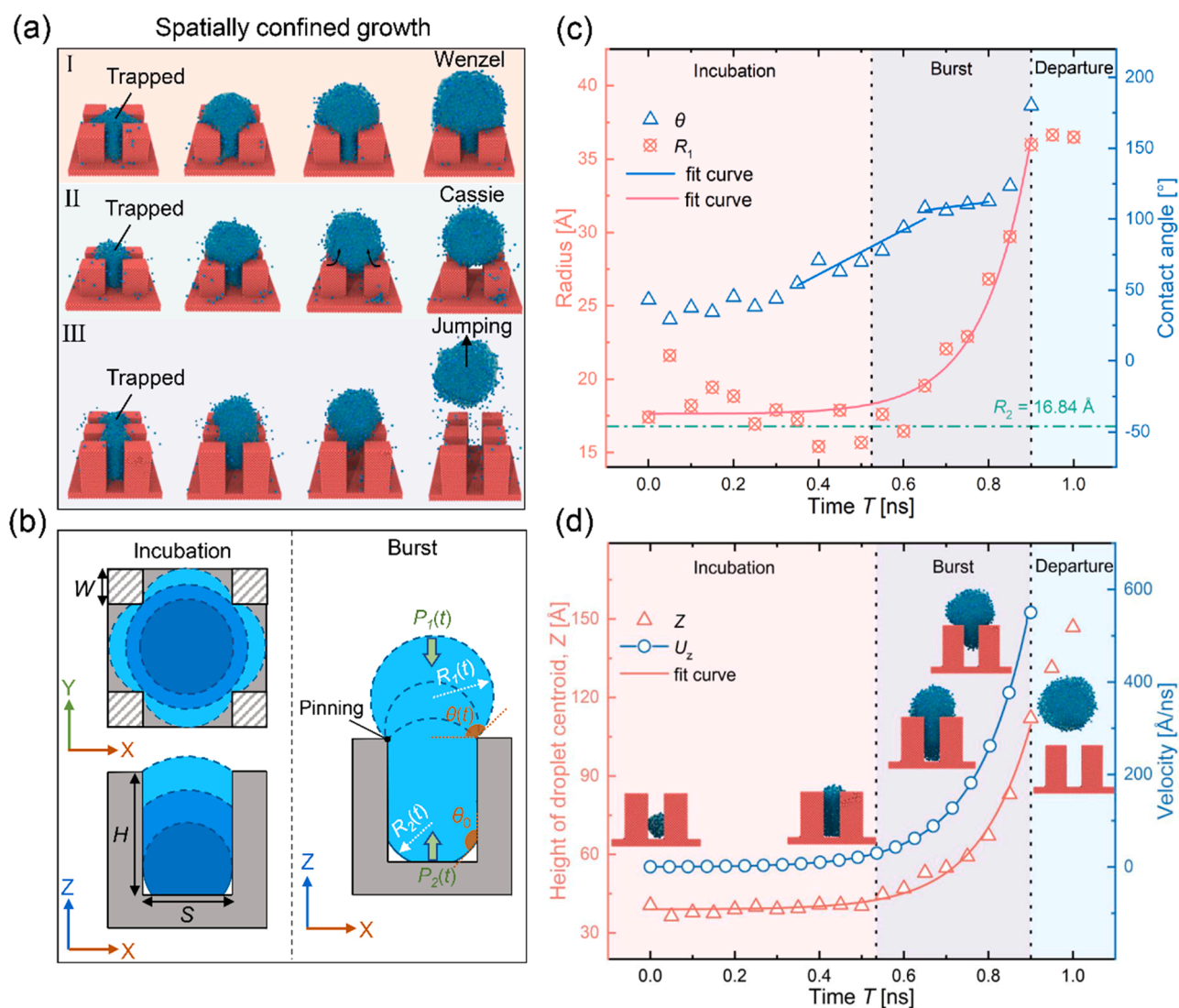
Fig. 3. (a) Spatially-confined growth modes of an isolated droplet on different nanopillar surfaces: growth-induced dewetting transition and self-jumping without any coalescence events. The corresponding pillar properties of each case are listed in Table S3 in SI. (b) Schematic of the growth process, the squeezed droplet grows upwards firstly until it emerges from the pillars valley (the incubation stage), and followed by the rapid expansion of droplet head (the burst stage). (c) Temporal evolutions of the apparent dynamic contact angle θ and the curvature radius R_1 at the upper liquid-vapor interface of the growing droplet, the curvature radius R_2 at the bottom interface is estimated to be $S/2\cos(\pi - \theta_0)$. (d) Droplet centroid height Z and vertical velocity U_Z as a function of time. Insets illustrate the typical position and morphology of the growing droplet in each corresponding stage.

spherical-cap shape, but become deformed immediately as the growing droplet touches the sidewalls of nanopillars. After filling the footprint of the unit cell, the confined droplet grows upward until its top interface exceeds the upper edge of pillars, and then the bulging droplet head (bulb) starts to expand both laterally and vertically, free from the constraint of the structures. But unexpectedly, the further growth of the droplet bulb leads to various state transitions, the droplet body might still be trapped inside structure valley (impaled Wenzel state, mode I), also might be pumped to structure tops (suspended Cassie state/dewetting transition, mode II) or even be ejected from the surface (self-jumping, mode III). We have to emphasize that the droplet grows separately without any disturbance; moreover, the status of the growing droplet on each surface is not exactly the same. Hence, it is reasonable to conclude that these different outcomes are relevant with the surface structure properties.

Fig. 3b schematically shows the above spatially-confined growth process, whose dynamic evolution is also visualized by the time-lapse snapshots in Fig. 3d. In the early incubation period with the droplet being fully embedded in the pillar valley, upward growth is more energetically favorable *versus* sideways inflation [30], and the droplet shape could be approximated as an axisymmetric cylinder bounded by the rectangular pillars at the corners. Once the longitudinal triple-phase contact line reaches the height of pillars, the curvature radius of top interface R_1 increases with the inflating droplet bulb whose base is pinned at the pillar top edges, while the curvature radius of bottom interface R_2 still remains unchanged, that will generate an upward Laplace pressure difference ΔP [57–59] (it has been experimentally found that, the square-shaped structures may also provide a pressure gradient within a droplet [58,60–62], besides the diverging cavity geometries [63,64]). When the droplet bulb grows to a certain size, the driving force is large enough to overcome the surface adhesion force, and further triggers the detachment of the squeezed droplet body from structure valleys.

To corroborate the above force analysis, the curvature radius R_1 and the dynamic contact angle θ (as marked in Fig. 3b) were extracted from the droplet morphology, as shown in Fig. 3c. In the incubation stage, the value of R_1 (17.78 Å) obtained from the fitting data is roughly equal to the calculated value of R_2 (16.84 Å) estimated as $S/2\cos(\pi-\theta_0)$ (the bottom portion of the tail is assumed to be a spherical cap as shown in Fig. 3b, so the curvature of the bottom tail can be estimated as $S/2\cos(\pi-\theta_0)$), but this balance is soon disturbed in the later burst stage. As the growing droplet emerges from the valley, R_1 increases dramatically with the fast expansion of the droplet bulb, in contrast, R_2 stays almost constant under the shape restriction from structures. As a result, the steady increase in curvature difference leads to an ever-increasing Laplace pressure difference ΔP ($\Delta P = P_2 - P_1 \approx 2\sigma(1/R_2 - 1/R_1)$, given the curvature difference in the XZ-plane is approximately equal to that in the YZ-plane). Furthermore, from the visualized droplet shape and the fitting curve of R_1 and θ, it is observed that the droplet bulb grows in a constant contact line (CCL) and a constant contact angle (CCA) mode successively, which can be elucidated by a local force analysis [65,66]. Initially when the droplet bulb exceeds the top face of pillars, its contact line is confined due to the pinning effects from the pillar edges. As a result, the droplet growth compels the dynamic contact angle θ to rise rapidly (the contact radius R_c remains constant) and thus provide an increasingly powerful depinning force $F_D = 2R_c\sigma(\cos\theta - \cos\theta_0)$. As θ increases to a critical value, *i.e.*, the advancing contact angle θ_A, F_D can overcome the pinning force F_P to move the contact line, leading to a both lateral and vertical expansion of the droplet bulb with a roughly unchanged dynamic contact angle θ.

To investigate the dynamics of the growth-induced self-jumping, the height Z and the vertical velocity U_Z of centroid were extracted from the droplet trajectory. As shown in Fig. 3d, both of them remain constant initially and then increase in time with a power-law relation. In the burst period, the rapid retraction of the droplet tail causes a sharp increase in Z and U_Z, and the vertical velocity of the droplet tail U_t is significantly

higher than that of the droplet bulb U_b (see Fig. S12 in SI), due to the pinning effects on the droplet tail that is initially adhered to the structure valley floor. The pinning force hinders the detachment of droplet tail and further stretches the droplet body, until the growing droplet bulb attains a sufficient Laplace pressure difference. Then, the abrupt depinning of the droplet tail triggers an explosive retraction of the originally elongated droplet body, and the consequent upward flow and momentum propel the droplet bulb to move.

Fig. 4a is a phase diagram of the three growth modes. *i.e.*, Wenzel, Cassie and self-jumping, as a function of the pillar topography (the dimensionless spacing $S^*(S/W)$ and height $H^*(H/W)$) and wettability (the intrinsic contact angle θ_0) based on all the numerical simulation cases, refer to Table 1 for corresponding pillar properties of each surface. From this figure, one can know how to design the surface roughness to effectively control the wetting state of a growing droplet. The droplet undergoes Wenzel state, Cassie state and self-jumping state successively, with the decrease of S^* or with the increase of H^* and θ_0, so we can deduce that the tall and dense nanostructures with a good hydrophobic performance could intensify the mobility of droplet, which is attributed to the competition between the excessive surface energy stored in the deformed droplet and the frictional dissipation at the interface. Additionally, to provide an energic insight into these diverse wetting states, we conducted an energy analysis on the spatially-confined droplet growth.

In terms of energy arguments, the deformed droplet possesses a larger surface area compared to the spherical droplet with an identical volume. It follows that an excessive surface energy is stored in the squeezed droplet caused by the spatial confinement of the pillar sidewalls, as a result, the spherical shape is energetically favorable and the released surface energy might be partially converted into the kinetic energy during the shape recovery. To clarify the relations between the critical (minimum) self-jumping size and the nanostructure properties, a two-stage energetic model was proposed to describe the confined growth of an isolated droplet, as shown in Fig. 4b. The droplet is initially trapped inside a unit cell, and our model first considers the transition point between these two stages, where the deformed droplet is approximated as an incomplete cylinder and its top interface just reaches the upper edge of pillars. The calculations of surface energy changes demonstrate that the droplet prefers to grow upward rather than expand laterally at this moment due to the lower energy cost [30], and the value of droplet radius r_p can be obtained numerically based on minimum free energy (see section S6 in SI for detailed derivation). Subsequently, the droplet bulb starts to inflate into the air and its base is pinned at the pillar top edges, *i.e.*, the droplet bulb grows in a constant contact line (CCL) mode with a pinned contact radius r_p, so the apparent contact angle θ can be described by the droplet bulb radius R as $\theta = \sin^{-1}(r_p/R)$ in the inflation stage, as shown in Fig. 4b. Supposing the droplet grows to a critical size and departs from the surface eventually, then its self-jumping behavior follows the energy-balance equation [45], namely $\Delta E_S = E_k + E_{adh} + E_{vis} + E_{cl}$, where ΔE_S, E_k, E_{adh}, E_{vis} and E_{cl} are the released surface energy, the kinetic energy of jumping droplet, the adhesion work, the viscous dissipation and the contact-line dissipation, respectively. By calculating all of above energy terms (see Section S6 in SI for detailed calculations), we obtained the critical (minimum) self-jumping radius R_m and contact angle θ_m of the confined droplet, which are dependent on the nanopillar topology, as shown in Figs. 4c and 4d. The result suggests that both R_m and θ_m decrease with an increasing pillar height H or a decreasing pillar spacing S, that is, sufficiently tall and dense nanopillars serve to improve the excessive surface energy and further prompt the trapped droplet to change its wetting state, which is consistent with the aforementioned simulation results.

3.3. Coalescence-induced transition

Following the spatially-confined growth having three modes, the two
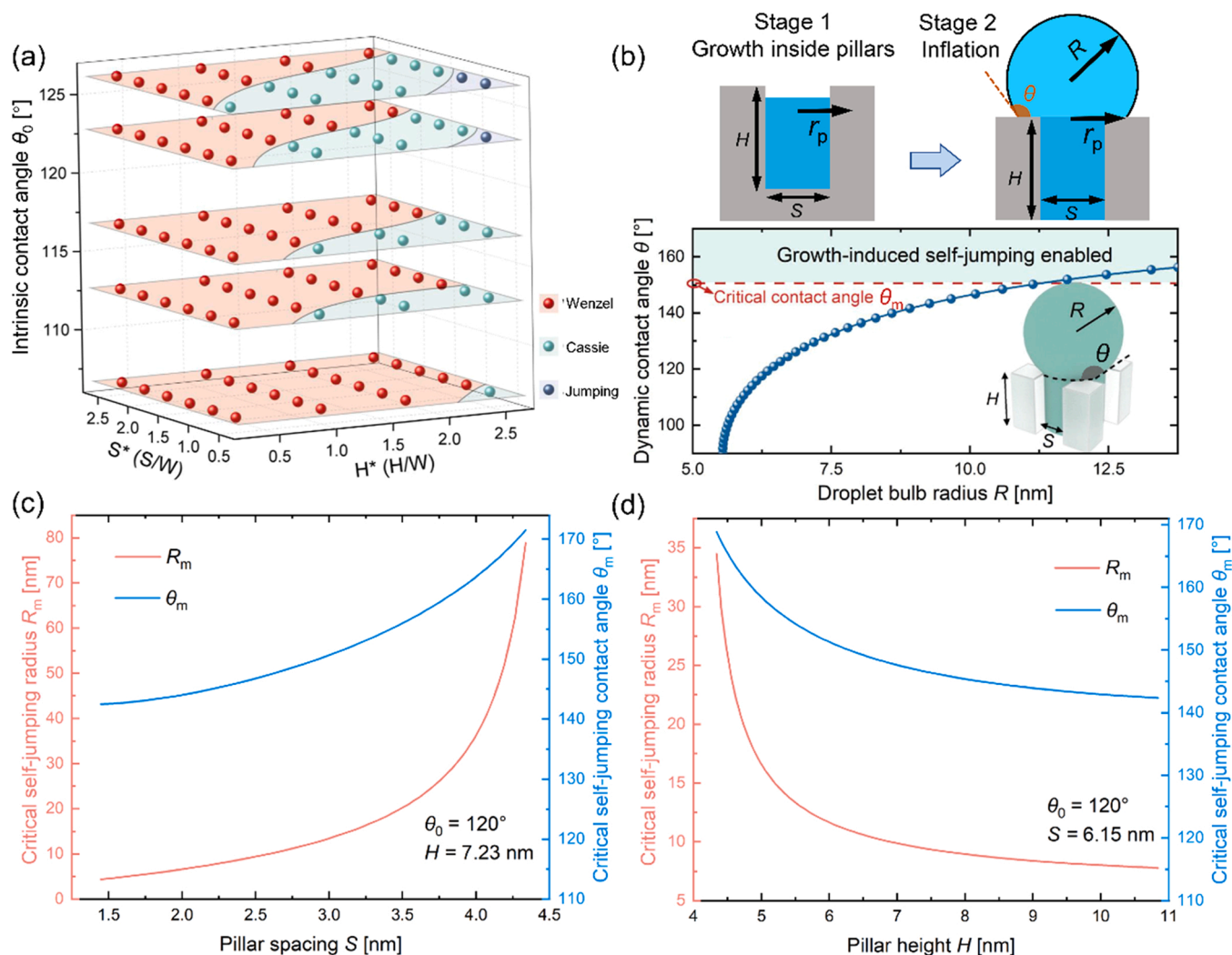
Fig. 4. Different droplet growth modes and the energetic analysis. (a) Three-dimensional regime map of spatially-confined droplet growth as a function of the surface structure topography ($W = 3.1$ nm, $S^* = S/W$, $H^* = H/W$) and wettability (intrinsic contact angle θ_0) based on all the numerical simulation cases. See Table 1 for detailed properties of each surface. (b) Schematic of the confined growth process involving an incubation stage (growth inside pillars) and a burst stage (inflation atop pillars), and evolution of the apparent dynamic contact angle θ for the droplet head during the burst stage. (c) Dependences of the critical (minimum) self-jumping radius R_m and contact angle θ_m of confined droplet on the pillar spacing S (intrinsic contact angle $\theta_0 = 120°$, pillar height $H = 7.23$ nm). (d) Dependences of the critical (minimum) self-jumping radius R_m and contact angle θ_m of confined droplet on the pillar height H (intrinsic contact angle $\theta_0 = 120°$, pillar spacing $S = 6.15$ nm).

adjacent droplets merge with each other, thereby leading to a more diverse set of outcomes on different nanopillar surfaces, as shown in Fig. 5. Noted that they are rarely noticed and discussed in previous experimental evidences, and we classified them into four regimes according to the initial state of droplet. Since the nucleated droplets tend to grow within structures, the coalescence events usually start between two small Wenzel droplets (mode I), as shown in Fig. 5a, and the newly formed droplets present three distinct wetting states (Wenzel, Cassie or jumping) under different solid-liquid interface interactions (see Video S3 in SI). In addition, the small Wenzel droplet may also merge with a slightly larger Cassie droplet (mode II) that derived from the growth- or coalescence-induced state transition of a small Wenzel droplet, and further transform into a large Cassie droplet or even depart from the surface (Fig. 5b, see Video S4 in SI). Soon afterwards, the resultant flying droplet might touch and assimilate other sessile Wenzel or Cassie droplets around its flight path (mode III), and stimulate them to change their status again or jump out-of-plane (Fig. 5c, see Video S5 in SI). Finally, it comes to the coalescence of two Cassie droplets (mode IV) that has been often observed in previous studies, the coalesced large droplet might remain its original wetting state or will probably lead to a jumping

as well (Fig. 5d, see Video S6 in SI). Furthermore, the coalescence-induced transition also occurs among the multiple droplets with various states (see Fig. S20 and Video S7 in SI).

The above findings complement the experimental observations and improve the understanding for the droplet morphology evolutions, indicating that the jumping-droplet condensation actually consists of multifarious state-transition and self-jumping events occurring among various droplets, rather than as a unitary pattern dominated by the coalescence-induced jumping of Cassie droplets. Moreover, it is interesting to note that the final wetting state of a condensed droplet seems more like a chain-reaction result of these sequential nucleation-growth-coalescence events, and our simulations suggest that the nanopillar surface with low solid fraction and strong hydrophobicity generally endows the condensed droplets with a good mobility (suspended Cassie state or coalescence-induced jumping), and the reason will be discussed later in this study.

Considering the jumping events were observed to usually occur between Cassie droplets in previous experimental evidences, thus the nanoscale Cassie-Cassie jumping case in Fig. 5d was selected to compare the differences in dynamic characteristics of droplet coalescence (the
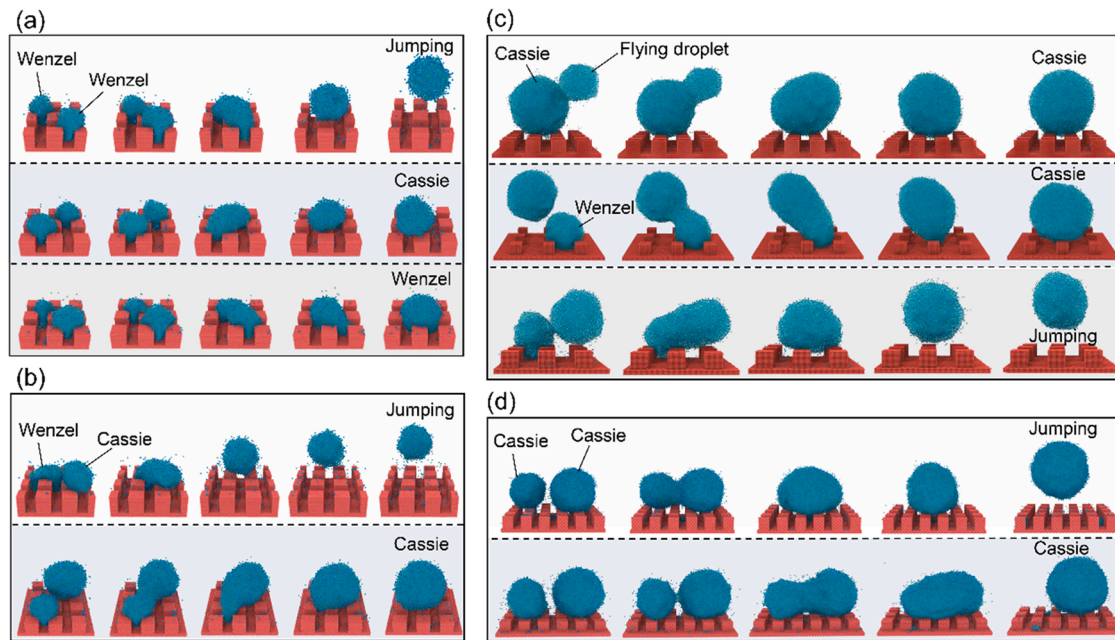
Fig. 5. Comparison of the time-lapse snapshots for the condensed droplet coalescence modes on different nanopillar surfaces. All of these two-droplets coalescence events may potentially cause a spontaneous jumping or a dewetting transition. (a) Mode I, Wenzel-Wenzel droplets coalescence. (b) Mode II, Wenzel-Cassie droplets coalescence. (c) Mode III, coalescence between a flying droplet and a sessile droplet. (d) Mode IV, Cassie-Cassie droplets coalescence. The corresponding pillar properties for above all cases are shown in Tables S4-S7 in SI respectively.

coalescence dynamics of Wenzel-Wenzel droplets is discussed in Section S9 of SI), one can notice that there is no obvious interface oscillation for the coalescing nanodroplet. This is because the droplet dynamics is governed by the inertial, surface tension and viscous forces comprehensively [67], and the viscous effect gradually replaces the inertia effect and becomes dominated as the spatial scale decreases [68]. As a result, the liquid-gas interface of a nanodroplet fluctuates very slightly. Based on the position coordinate of the droplet centroid, we calculated the vertical velocity of the coalesced droplet U_Z and the horizontal radial velocity of each droplet, U_{X1} and U_{X2}. Figs. 6a and 6b respectively show their temporal evolutions, which could be divided into four phases according to the corresponding droplet morphology visualized in the insets. Starting from the formation and expansion of the liquid bridge (0–0.1 ns), the centroid height is lowered ($U_Z < 0$) as the liquid mass migrates toward the center ($U_{X1} > 0$, $U_{X2} < 0$) driven by the Laplace pressure. When the downward-moving liquid bridge contacts and impacts the substrate, the coalesced droplet accelerates upwards until U_Z reaches the maximum value of 0.17 Å/ps at 0.25 ns, and the lateral retraction slows down simultaneously (both U_{X1} and U_{X2} decrease). During the subsequent droplet detachment, U_Z decelerates to a critical value ~ 0.08 Å/ps (the jumping velocity U) at 0.45 ns under the adhesion force exerted by surface. Meanwhile, the direction of U_{X1} and U_{X2} are inverted symmetrically, accompanied by a periodic oscillation of the coalesced droplet. At last (> 0.45 ns), the horizontal radial velocities attenuate to zero, and the kinetic energy of departing droplet is dissipated gradually due to the resistance from vapor particles and clusters. It should be noted that the variations of U_{X1} and U_{X2} show a reversed-phase oscillation in general, but the velocity amplitudes are inconsistent because the mass of each coalescing droplet is different (the diameters $D_1 \approx 13$ nm, $D_2 \approx 15$ nm).

Furthermore, another simulation was performed to probe the internal fluid flow characteristics of a coalescing droplet (see section S10 in SI for simulation details). The entire simulation region was divided into many cubic boxes with a side length of 20 Å, and the time-averaged local properties of each box, including fluid density and velocity, were calculated and recorded at regular intervals, then a X-Z central cross section was chosen to plot fluid density contour, velocity field and

stream filed, as shown in Fig. 6c and Fig. S15 respectively. It is clearly observed from the stream field (Fig. S15 in SI) that, there initially exist both upward and downward motions in the expanding liquid bridge at t_0. But soon after, the downward velocity decreases and reverses its direction at $t_0 + 2\Delta t$ due to the impact of liquid bridge, and the surface-liquid interactions endow the droplet with an overall upward momentum eventually ($t_0 + 5\Delta t$), which indicates an imminent jumping.

Generally, the droplets coalescence on a surface follows the energy-conservation principle, however, the existing models developed from the basic energy-balance equation, $\Delta E_s = E_{adh} + E_{vis} + E_k$, mostly treat the surface underneath droplets as smooth because of its relatively small feature size of roughness [27,69–72]. Hence, they overlook the role of the underlying surface structure, which will be more prominent as the droplet size descends. Furthermore, the above visualization results indicate that the state transitions induced from coalescence are varied with the structure topography and wettability, so we propose a modified model to rationalize this relationship and extend the prediction of the jumping velocity to the nanometric length scale. Given the coalescence process of two same-sized droplets sitting on the nanopillar arrays, as schematically shown in Fig. S16 of SI, the initial total surface energy could be evaluated as

$$E_S = 2\left[2\pi(1 - \cos\theta)R^2\sigma_{LV} + \pi(R\sin\theta)^2(1 - \varphi_s)\sigma_{LV} + \pi(R\sin\theta)^2\varphi_s\sigma_{SL}\right] \quad (2)$$

where the apparent contact angle θ can be obtained by the Cassie-Baxter equation $\cos\theta = \varphi_s(\cos\theta_0 + 1) - 1$ and θ_0 is the intrinsic contact angle, $\varphi_s = W^2/(W+S)^2 = 1/(1 + S^*)^2$ is the surface solid fraction, R is the radius of each droplet, σ_{LV} and σ_{SL} are the liquid-vapor and solid-liquid surface tensions, respectively. By contrast, the total surface energy after coalescence-induced jumping could be calculated as $E_S{}' = 4\pi(R')^2\sigma_{LV} + 2\pi R^2\sin^2\theta\varphi_s\sigma_{SV}$, where the final radius of the coalesced droplet $R' = \sqrt[3]{\frac{2 - 3\cos\theta + \cos^3\theta}{2}}R$ is calculated on the basis of the volume conservation, then we can obtain the available excessive surface energy $\Delta E_S = E_S - E_S{}'$, The surface adhesion work E_{adh} could be expressed by Young-Dupre equation
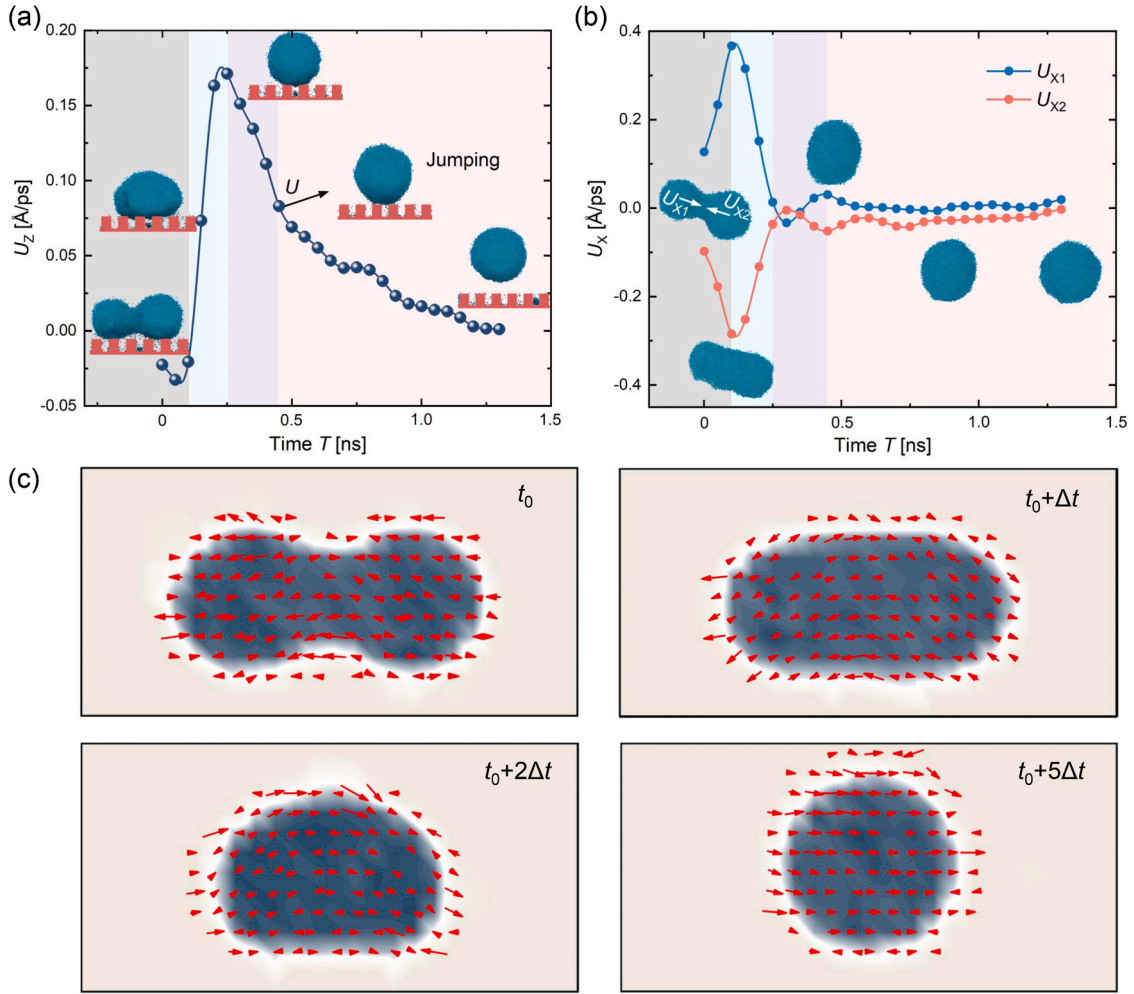
Fig. 6. Dynamic analysis on the coalescence-induced jumping of condensed nanodroplets. (a) Temporal variation of the vertical centroid velocity U_Z. The series of snapshots show the typical droplet morphology in these four specific stages (front view). (b) Temporal variation of the horizontal radial velocity for each droplet, U_{X1} and U_{X2}. Insets visualize the morphology evolution of the coalesced droplet (top view). (c) Representative fluid density contour and velocity field at the X-Z central cross section (stream field is shown in Fig. S15 of SI).

$$E_{adh} = 2\pi R^2 \sin^2\theta(1 + \cos\theta)\varphi_s\sigma_{LV} \tag{3}$$

The viscous dissipation E_{vis} is mainly incurred by the elaborated internal flow in the droplet (fluid convection or diffusion), and could be estimated as [27].

$$E_{vis} = 2\int_0^{\tau_{vis}} \int_V \Phi dV dt \approx 2\Phi V \tau_{vis} \tag{4}$$

where $V = \pi(2 - 3\cos\theta + \cos^3\theta)R^3/3$ is the volume of each droplet, τ_{vis} is the viscous dissipation time, and Φ is the dissipation function. It has been confirmed that the viscous dissipation during coalescence is dominated by the droplet lateral motion, and thus the dissipation function Φ is estimated to be

$$\Phi \approx \frac{1}{2}\mu(\frac{U_x}{R})^2 \tag{5}$$

where μ is the liquid dynamic viscosity, U_x is the average merging velocity in the lateral direction, which could be estimated as [73].

$$U_x \approx 2(\theta + \sin\theta\cos\theta)\sigma_{LV}R \bullet \tau_{vis}/\rho V \tag{6}$$

for the convenience of calculation, the dissipation time τ_{vis} is approximated by the coalescence time τ, which is given by [28].

$$\tau = \frac{\mu r_c}{\sigma_{LV}} + \left[\frac{\rho}{\sigma_{LV}D_0{}^4}\right]^{1/2} \bullet (R^{3/2} - r_c{}^{3/2}) \tag{7}$$

where ρ is the liquid density, the constant D_0 is taken as 1.39, and $r_c \approx 8\mu\sqrt{R/(\rho\sigma_{LV}D_0{}^4)}$ is the critical bridge radius at the viscous-to-inertial regime transition moment. As such, the viscous dissipation E_{vis} can be obtained by substituting Eqs. (5)–(7) into Eq. (4).

However, the basic energy-balance equation mentioned above is incompetent to exactly describe the coalescence of nanodroplets, and some extra nano-physical effects need to be considered in the energy analysis. Most of previous models assumed the viscous dissipation of liquid bulk E_{vis} as the only source of energy dissipation in macroscale. However, with the shrink of spatial scale, the contact-line movement is determined by the forward and backward jumping frequencies of liquid molecules in the contact area from the perspective of molecular kinetic theory (MKT) [74]. Thus, the energy dissipation caused by contact line friction E_{cl} becomes prominent in nanoscale droplet movement, which is determined by the contact-line friction coefficient μ_{cl}, the characteristic contact-line velocity u, the characteristic length L and the contact-line dissipation time τ_{cl}, given by [75].

$$E_{cl} \approx \mu_{cl}u^2L\tau_{cl} \tag{8}$$

where μ_{cl} could be approximated by μ, u is on the same order of magnitude as U_x, L is defined as distance between the two initial droplet-surface contact points, here, $L \sim 2R$, and τ_{cl} could be approximated by τ. Furthermore, as the droplet size approaches to nanoscale, the line tension σ_κ, the excess of free energy per unit length of the triple-phase contact line, also becomes non-ignorable owing to the increasing line-to-surface ratio in the small droplet. Thus, the energy dissipation caused by line tension E_{lt} should be considered and could be evaluated as [45].

$$E_{lt} = 2\sigma_\kappa L_{lt} \qquad (9)$$

where L_{lt} is the total contact line length of single droplet, which is contributed by the internal contact line $L_{in} = 4\pi W \left(\frac{R\sin\theta}{(S+W)}\right)^2$ and the contact line boundary $L_{ex} \approx 1.738\pi R\sin\theta \frac{W}{(S+W)^2} \bullet (2.184W + 0.288\pi W)$, σ_κ is the line tension coefficient, and its value is still a subject to controversy, which has been reported to span over seven orders of magnitude,

ranging from 10^{-12} J/m to 10^{-5} J/m. It is now generally accepted that the line tension has a magnitude of 10^{-11}-10^{-10} J/m [51,52,76,77], and shows a dependence on surface wettability [78]. Our model mainly considers the droplet jumping velocity for a hydrophobic surface (intrinsic contact angle $=120°$ and apparent contact angle $\approx 150°$), which exbibits a similar wettability compared to the smooth fluoropolymer-coated surface (intrinsic contact angle $\approx 115°$ and line tension $= 2 \times 10^{-10}$ J/m) [45], thus we approximatively specified the line tension as a constant with a value of 2×10^{-10} J/m here.

In addition, it should be stressed that the total kinetic energy E_k of coalesced droplet contains the translational part $E_{k,tr}$ and the oscillatory part $E_{k,os}$, while the jumping behavior is powered by the $E_{k,tr} = \frac{mU_j^2}{2}$, where m is the mass of coalesced droplet and U_j is the jumping velocity, and the proportion of $E_{k,tr}$ in E_k is given by a piecewise function $g(Oh)$ of the Ohnesorge number $Oh = \mu/\sqrt{\rho\sigma_{LV}R}$ [32]. Finally, combining all of these energy items yields a modified energy-based model (see fully detailed derivation in Section S11 of SI)
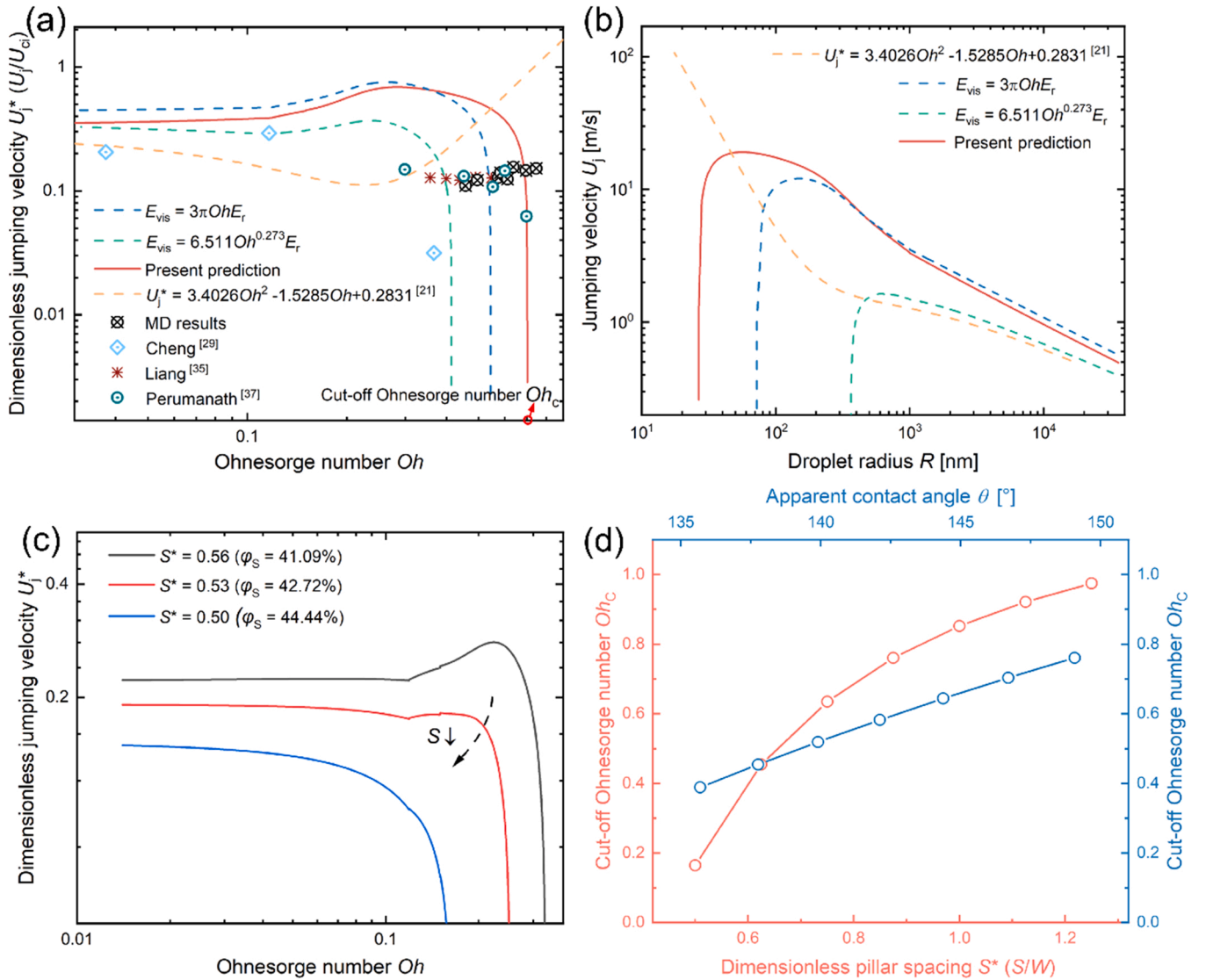
Fig. 7. Theoretical prediction for the jumping velocity of coalesced droplet in the nanometer to micrometer size. (a) Variations of the scaled jumping velocity U_j^* with the Oh number based on the present predictions and MD simulations, previous theoretical predictions, numerical simulations and experimental measurements. Here, $Oh_C = \mu/\sqrt{\rho\sigma_{LV}R_C}$ is the cut-off Oh number corresponding to the minimum jumping size R_C. (b) Variations of the jumping velocity U_j with the droplet radius R based on the present predictions and previous theoretical models. (c) Evolution of the varying tendency of $U_j^* - Oh$ curve, which gradually degenerates into a simple monotonic curve as the pillar spacing S decreases or surface solid fraction φ_s increases. (d) Dependence of the cut-off Oh number Oh_C on the surface structure topography (dimensionless pillar spacing S^*) and wettability (apparent contact angle θ).

$$E_{k,tr} = g(Oh)(\Delta E_s - E_{adh} - E_{vis} - E_{cl} - E_{lt}) \qquad (10)$$

which formulates the dependence of the jumping velocity U_j on the surface structure topology (W, S) and wettability (θ) and the droplet size R (or the Oh number).

Fig. 7a shows the variation of the inertial-capillary scaled jumping velocity U_j^* ($U_j^* = U_j/U_{ci}$, $U_{ci} = \sqrt{\sigma/\rho R}$) with the Oh number by the present predictions and MD simulation results, for a given nanopillar surface with $S^* = 0.875$, $H^* = 1.375$ and apparent contact angle $\theta \approx 150°$ (intrinsic contact angle $\theta_0 = 120°$), and the variation of the dimensional jumping velocity U_j with the droplet radius R is shown in Fig. 7b correspondingly. It can be noticed that the present model matches well with other theoretical curves in low Oh range (for micrometer-sized droplets), but the values of U_j^* obtained from the MD simulations are generally lower than their theoretical predictions. This is because these jumping cases are extracted from the condensation processes where the droplets grow naturally and thus have unequal radii, the kinetic energy conversion efficiency is reduced due to the size mismatch effect, however, that is not the primary reason (see additional MD simulations on the coalescence-induced jumping of two same-sized nanodroplets, Section S12 in SI). For a coalescing nanodroplet, its kinetic energy will be dissipated by the ambient gas significantly because of the low Knudsen number. Furthermore, although the present theoretical model has included the nano-physical items E_{cl} and E_{lt}, there still exist some other molecular physics that have not been considered, such as the energy dissipation caused by the drag from surrounding gas during coalescence, the thermal fluctuations at the interface and the temperature rise during coalescence [37]. All above mentioned factors result in the deviations between present theoretical predictions and MD results collaboratively.

Compared with two previous theoretical models where the viscous dissipation E_{vis} is given by $E_{vis} = f(Oh)E_r$ ($E_r = \sigma_{LV}R^2$ is a reference energy, the $f(Oh)$ is respectively a power law formula $6.511Oh^{0.273}$ [32] and a linear form $3\pi Oh$ [43]), our present model predicts a wider range of Oh for the possible coalescence-induced jumping, that is, the minimum jumping-droplet radius R_c could reach the nanoscale (about tens of nanometers, see Fig. 7b), which basically agrees with our MD results and other numerical simulations. But it should be noted that in our model, the predicted U_j^* first increases rapidly, and then declines slowly and becomes relatively stable as Oh decreases, which is quite distinct from the common monotonically increasing tendency and should be attributed to the regulatory effects of surface structures that haven't been considered before. The previous classical models mostly treat the surface underneath droplets as smooth and neglect the role of the underlying surface structure, therefore the dimensionless jumping velocity U_j^* was predicted to be changed monotonically with the Oh number. Conversely, our present model associated the jumping velocity with Oh number and surface structure properties comprehensively, which is more reasonable on the micro-nanoscale. Since the structure size is comparable to the drop characteristic dimension at this situation, and thus the surface should be regarded as rough one. Fig. 7c shows different $U_j^* - Oh$ curves for surfaces with different structure spacings, and it can be observed that, with the decrease of the dimensionless pillar spacing S^* or with the increase of the surface solid fraction $\varphi_s = 1/(1 + S^*)^2$, the nanopillar arrays look increasingly like a smooth surface, and consequently the complicated $U_j^* - Oh$ curve gradually degenerates into a simple monotonic curve that can be regarded equivalent to these classical theoretical models, which corroborates that the surface structure play a prominent role in droplet jumping dynamics. Fig. 7d shows the relations of Oh_C with the surface apparent contact angle θ and the dimensionless pillar spacing S^*. Here, Oh_C is the critical (cut-off) Ohnesorge number corresponding to the critical (minimum) jumping-droplet radius R_c, and can be used to evaluate the difficulty of the coalescence-induced jumping for different surfaces. It is seen that Oh_C is approximately proportional to θ,

and also follows a positive power-law relationship with S^*, which theoretically validates that the coalescence-induced jumping is highly dependent on the topology and wettability of surface nanostructure. Also, it suggests that rationally designed slender nanostructures with a good hydrophobicity and a low solid fraction would facilitate the departure of smaller droplets and even enable nanometric jumping.

4. Discussions

The present study reveals that all stages of the droplet lifecycle have a domino (cascade) effect on the final wetting morphology of a condensed droplet, which could provide a novel strategy to prevent the flooding phenomenon. Owing to the liquid retention within structures at a large surface subcooling, the resultant pinned Wenzel droplets cause the jumping-droplet condensation degrade into flooding condensation [79]. Conversely, both the confined-growth induced dewetting transition/departure and the coalescence-induced dewetting transition/jumping exhibit a great potential of draining condensates from surface structure gaps in this study. Therefore, these series of self-propelled droplet behaviors can be utilized for sequentially manipulating the transport of condensates, facilitating the mobile Cassie droplets formation, overcoming the surface flooding and further achieving a stable jumping-droplet condensation, which can be termed as cascade jumping-droplet condensation.

Although the cascade effect is promising to realize a stable jumping-droplet condensation over a wide range of subcooling, it still needs more in-depth studies to address some challenges for practical applications. For instance, how to guarantee the preferential nucleation between adjacent nanostructures at a low supersaturation. According to the classical nucleation theory, we calculated the average distance between nucleation sites l_c (see section S4 in SI for calculation details). The results show that l_c decreases with the increasing surface subcooling ΔT (Fig. S7), and to achieve the nucleation in adjacent unit cells with a spacing of ~5 nm, the surface subcooling should be larger than about 10 K (supersaturation > 1.76). Furthermore, as shown in Fig. 8a, we simulated the condensation processes on a superhydrophobic nanopillar surface at 300 K under different conditions of supersaturated water vapor, it can be found the nucleation within nanostructures is harder to achieve for a low supersaturation or surface subcooling. An attractive method to solve this problem is to utilize the biphilic surface consisting of hydrophilic patterns and superhydrophobic substrate. By introducing hydrophilic spots at the nanostructure valley floor, the steam will prefer to diffuse into structures and nucleate at the hydrophilic spots due to the lower free energy barrier. More interestingly, as shown in Fig. 8b, the resultant droplet is constrained inside the structures with its bottom contact lines pinned at the hydrophilic spot. As a result, the growing droplet deforms more violently as compared with similar structures without the hydrophilic spot, and more excessive surface energy will be released when the stretched droplet detaches from the hydrophilic spot and regain a spherical shape, thus enhancing the self-jumping of a single droplet [58,61].

In our energy-based model for predicting the coalescence-induced jumping velocity, the line tension was approximatively specified as a constant value of 2×10^{-10} J/m. But its value is virtually dependent on the surface wettability, thus it is valuable to conduct a series of MD simulations in a follow-up study, to establish a function relationship between the line tension and the surface Young's contact angle. Then, the quantitative relationship could be substituted into this model to provide a more accurate jumping prediction for various surfaces with different wettability.

This study clearly confirms the existence of nanometric jumping-droplet condensation from simulations and theories, the minimum jumping-droplet radius R_c could reach the nanoscale and that may affect the condensation heat transfer performance. Therefore, we studied the effects of R_c on the overall surface heat flux theoretically (see section S13 in SI for calculation details). Based on the prior model [80], the
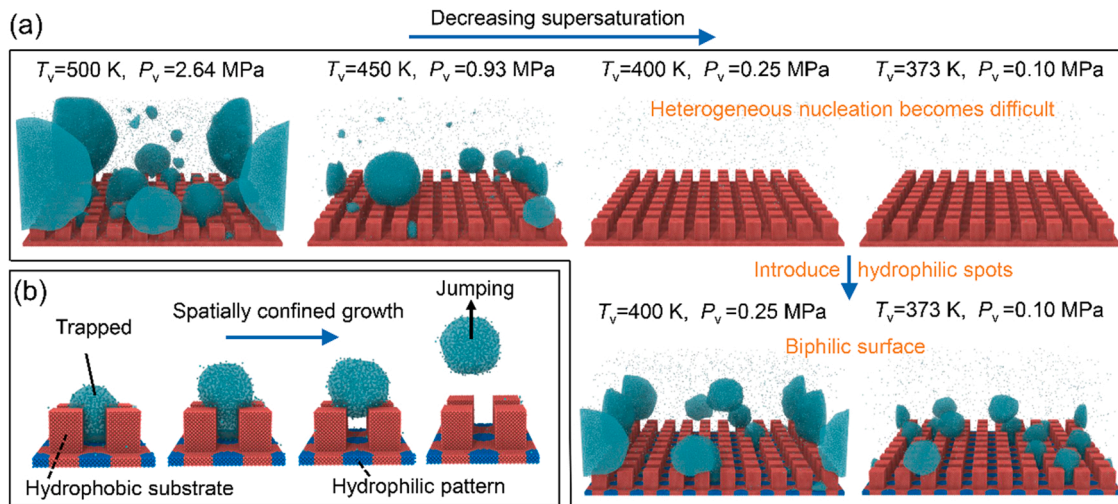
Fig. 8. (a) Condensation on a superhydrophobic nanopillar surface under different conditions of supersaturated vapor. The vapor becomes difficult to nucleate within adjacent nanopillars as supersaturation decreases, that can be solved by introducing the hydrophilic spots at the nanogroove bottom. (b) Self-jumping of an isolated growing droplet on the biphilic nanopillar surface ($T_v = 373$ K, $P_v = 0.10$ MPa).

overall heat flux q of the surface exhibiting coalescence-induced droplet jumping could be calculated as

$$q = \int_{R_{min}}^{R_e} q_d(R) n(R) d_R \tag{11}$$

where R_{min} is the critical droplet nucleation radius, $R_e = R_c$ is the droplet coalescence radius, q_d is the individual droplet heat transfer, n is the droplet population density and detailed calculation formulas are shown in section S13 of SI.

Fig. 9a shows the droplet size distribution $n(R)$ for a variety of droplet coalescence radii R_e, and these curves correspond to $R_e = 50$ nm, 100 nm, 300 nm, 500 nm, 1 μm, 3 μm, 5 μm, 10 μm, 15 μm and 20 μm. The droplets larger than the coalescence radius ($R > R_e$) are nonexistent due to the departure caused by droplet coalescence, which represents an ideal coalescence-induced droplet shedding. The results show that smaller R_e causes a higher droplet number density, and thus, the overall heat flux is improved accordingly, as shown in Fig. 9b.

5. Conclusions

In summary, we have studied the various self-propelled state-transitions and motions of nanoscale condensates on nanopillar surfaces with different topologies and wettability, by MD simulations and theory analysis. It is found that the nucleating embryos potentially evolve into the droplets with diverse morphologies, showing a domino (cascade) effect of all stages of the droplet lifecycle on the final wetting state. Due to the relatively low nucleation energy barrier, the liquid embryos prefer to incubate in the nanostructures and further grow up with their lateral expansion are restricted by the pillar sidewalls. The resultant squeezed droplets might behave the state transitions (Wenzel-Cassie dewetting transition or even self-jumping) under an asymmetric Laplace pressure that is affected by the nanopillar topography, and the energy analysis reveals that the minimum droplet self-jumping size decreases with increasing pillar height or decreasing pillar spacing, *i.e.*, tall and dense structures serve to store more excessive surface energy to facilitate the state transitions. And then, the multifarious coalescence events between these droplets lead to more diverse outcomes and probably trigger the
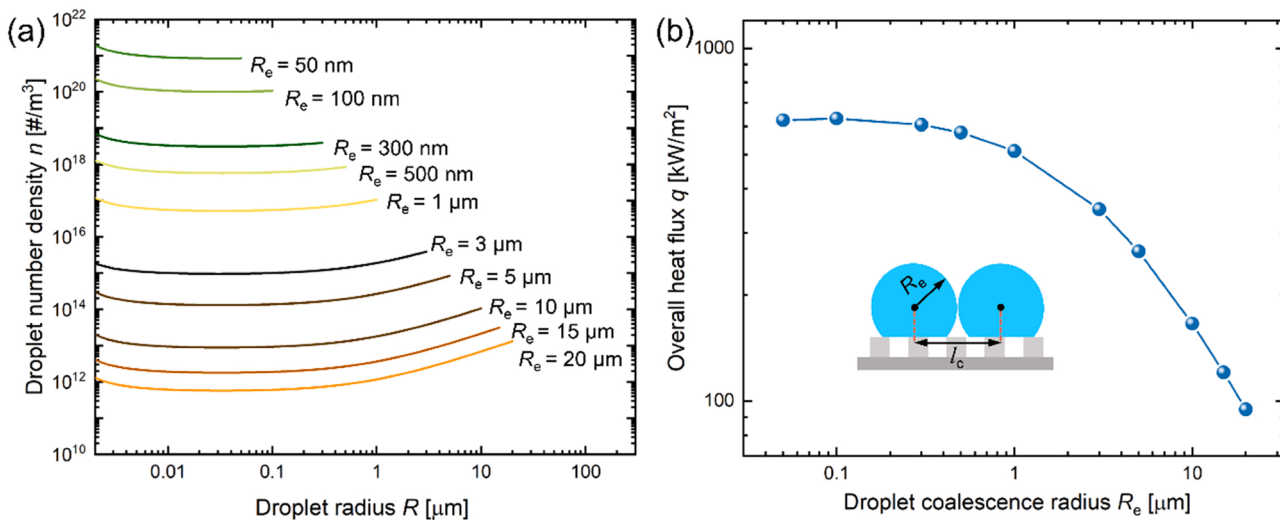

Fig. 9. (a) Droplet number density of jumping-droplet condensation as a function of droplet radius R for varying droplet coalescence radii R_e. larger R_e causes a wider range of droplet size distribution and a lower population density. (b) Overall jumping-droplet condensation heat flux as a function of coalescence radius R_e at surface subcooling $\Delta T = 20$ K. Inset: schematic showing droplet coalescence radius R_e and coalescence length $l_c = 2R_e$.

jumping as well, indicating the ultimate morphology of a condensed droplet is a chain-reaction result of these sequential nucleation-growth-coalescence events. By proposing a modified energy-based model considering both the underlying surface structure properties and nano-physical effects, we extend the prediction of jumping velocity to the nanometric length scale and find the slender nanostructures arrays with a low solid fraction could prompt the coalescence-induced jumping. This work reveals the insightful physical mechanisms of the micromorpho-logical evolutions of a condensed droplet over its entire lifecycle, and suggest that the jumping-droplet condensation is not actually a unitary pattern dominated by the coalescence-induced jumping. We hope that these findings could provide guidance for the surface nanofabrication to enable the directional transport and efficient removal of condensates, overcome the surface flooding and enable a steady cascade jumping-droplet condensation while also promoting droplet manipulation tech-niques and self-cleaning surface technology.

CRediT authorship contribution statement

Shan Gao: Conceptualization, Software, Investigation, Writing – original draft. **Jian Qu:** Methodology, Writing – review & editing. **Zhichun Liu:** Resources, Supervision. **Weigang Ma:** Funding acquisi-tion, Supervision.

Declaration of Competing Interest

The authors declare that they have no known competing financial interests or personal relationships that could have appeared to influence the work reported in this paper.

Data availability

Data will be made available on request.

Acknowledgement

Supporting Information

Simulation details including physical models, potential functions and control methods (Section S1); calculation and characterization of the intrinsic contact angle (Section S2); calculation of the nucleation energy barrier (Section S3); calculation of the nucleation density (Section S4); calculation of the potential energy distributions (Section S5); energy-based model of the confined-growth induced transition/departure (Section S6); energetic analysis for the preferential growth direction of confined droplet (Section S7); vertical velocity of the droplet bulb and droplet tail during self-jumping (Section S8); dynamics analysis of the coalescence-induced jumping for Wenzel droplets (Section S9); MD simulation for the internal stream field of a coalescing droplet (Section S10); energetic model of the coalescence-induced jumping on a nano-pillar surface (Section S11); simulations on the coalescence of two equal-sized droplets (Section S12); calculation for the overall condensation heat transfer (Section S13); pillar properties corresponding to Fig. 3a and Fig. 5 (Section S14); and visualization of spatially-confined growth, coalescence-induced jumping, jumping relay and sequential multi-droplet coalescence (Videos S1-S7 and Section S15).

Supplementary material related to this article can be found online at doi:10.1016/j.nanoen.2023.108558.

Appendix A. Supporting information

Supplementary data associated with this article can be found in the online version at doi:10.1016/j.nanoen.2023.108558.

References

[1] A.T. Paxson, J.L. Yague, K.K. Gleason, K.K. Varanasi, Stable dropwise condensation for enhancing heat transfer via the initiated chemical vapor deposition (iCVD) of grafted polymer films, Adv. Mater. 26 (2014) 418–423.

[2] W. Wang, Y. Shi, C. Zhang, S. Hong, L. Shi, J. Chang, R. Li, Y. Jin, C. Ong, S. Zhuo, P. Wang, Simultaneous production of fresh water and electricity via multistage solar photovoltaic membrane distillation, Nat. Comm. 10 (2019) 3012.

[3] M. Zou, Y. Zhang, Z. Cai, C. Li, Z. Sun, C. Yu, Z. Dong, L. Wu, Y. Song, 3D printing a biomimetic bridge-arch solar evaporator for eliminating salt accumulation with desalination and agricultural applications, Adv. Mater. 33 (2021), e2102443.

[4] J.M. Beér, Prog. High efficiency electric power generation: The environmental role, Energy Combust. Sci. 33 (2007) 107–134.

[5] T. Drew, W. Nagle, W. Smith, The conditions for dropwise condensation of steam, Trans. Am. Inst. Chem. Eng. 31 (1935) 605–621.

[6] J. Rose, P.I. Dropwise, condensation theory and experiment: a review, Mech. Eng. A-J. Pow. 216 (2002) 115–128.

[7] I. Tanasawa In *Critical size of departing drops*, Proceedings of 5th International Transfer Conference, 1974; p 188.

[8] D. Wang, Q. Sun, M.J. Hokkanen, C. Zhang, F.-Y. Lin, Q. Liu, S.-P. Zhu, T. Zhou, Q. Chang, B. He, Design of robust superhydrophobic surfaces, Nature 582 (2020) 55–59.

[9] H. Lambley, T.M. Schutzius, D. Poulikakos, Superhydrophobic surfaces for extreme environmental conditions, Proc. Natl. Acad. Sci. U. S. A. 117 (2020) 27188–27194.

[10] M. Jiang, Y. Wang, F. Liu, H. Du, Y. Li, H. Zhang, S. To, S. Wang, C. Pan, J. Yu, Inhibiting the Leidenfrost effect above 1,000° C for sustained thermal cooling, Nature 601 (2022) 568–572.

[11] J.B. Boreyko, C.-H. Chen, Self-propelled dropwise condensate on superhydrophobic surfaces, Phys. Rev. Lett. 103 (2009), 184501.

[12] M.J. Hoque, S. Chavan, R. Lundy, L. Li, J. Ma, X. Yan, S. Lei, N. Miljkovic, R. Enright, Biphilic jumping-droplet condensation, Cell Rep. Phys. Sci. 3 (2022), 100823.

[13] R. Wen, S. Xu, X. Ma, Y.-C. Lee, R. Yang, Three-dimensional superhydrophobic nanowire networks for enhancing condensation heat transfer, Joule 2 (2018) 269–279.

[14] X. Yan, B. Ji, L. Feng, X. Wang, D. Yang, K.F. Rabbi, Q. Peng, M.J. Hoque, P. Jin, E. Bello, S. Sett, M. Alleyne, D.M. Cropek, N. Miljkovic, Particulate-droplet coalescence and self-transport on superhydrophobic surfaces, ACS Nano 16 (2022) 12910–12921.

[15] K.M. Wisdom, J.A. Watson, X. Qu, F. Liu, G.S. Watson, C.-H. Chen, Self-cleaning of superhydrophobic surfaces by self-propelled jumping condensate, Proc. Natl. Acad. Sci. U. S. A 110 (2013) 7992–7997.

[16] H. He, Z. Guo, Superhydrophobic materials used for anti-icing Theory, application, and development, Iscience 24 (2021) 103357.

[17] H. Zhang, G. Zhao, S. Wu, Y. Alsaid, W. Zhao, X. Yan, L. Liu, G. Zou, J. Lv, X. He, Z. He, J. Wang, Solar anti-icing surface with enhanced condensate self-removing at extreme environmental conditions, Proc. Natl. Acad. Sci. USA 118 (2021).

[18] N. Miljkovic, D.J. Preston, R. Enright, E.N. Wang, Jumping-droplet electrostatic energy harvesting, Appl. Phys. Lett. 105 (2014), 013111.

[19] K.F. Wiedenheft, H.A. Guo, X. Qu, J.B. Boreyko, F. Liu, K. Zhang, F. Eid, A. Choudhury, Z. Li, C.-H. Chen, Hotspot cooling with jumping-drop vapor chambers, Appl. Phys. Lett. 110 (2017), 141601.

[20] T. Foulkes, J. Oh, P. Sokalski, L. Li, S. Sett, J. Sotelo, X. Yan, R. Pilawa-Podgurski, A. Castaneda, M. Steinlauf, Jumping droplets electronics cooling: Promise versus reality, Appl. Phys. Lett. 116 (2020), 203701.

[21] R. Enright, N. Miljkovic, J. Sprittles, K. Nolan, R. Mitchell, E.N. Wang, How coalescing droplets jump, ACS Nano 8 (2014) 10352–10362.

[22] R. Mukherjee, A.S. Berrier, K.R. Murphy, J.R. Vieitez, J.B. Boreyko, How Surface Orientation Affects Jumping-Droplet Condensation, Joule 3 (2019) 1360–1376.

[23] Y. Zhu, T.C. Ho, H.H. Lee, M.K.H. Leung, C.Y. Tso, Droplet jumping physics on biphilic surfaces with different nanostructures and surface orientations under various air pressure conditions, Cell Rep. Phys. Sci. 3 (2022), 100849.

[24] M.K. Kim, H. Cha, P. Birbarah, S. Chavan, C. Zhong, Y. Xu, N. Miljkovic, Enhanced Jumping-Droplet Departure, Langmuir 31 (2015) 13452–13466.

[25] X. Qu, J.B. Boreyko, F. Liu, R.L. Agapov, N.V. Lavrik, S.T. Retterer, J.J. Feng, C. P. Collier, C.-H. Chen, Self-propelled sweeping removal of dropwise condensate, Appl. Phys. Lett. 106 (2015), 221601.

[26] K. Rykaczewski, A.T. Paxson, S. Anand, X. Chen, Z. Wang, K.K. Varanasi, Multimode multidrop serial coalescence effects during condensation on hierarchical superhydrophobic surfaces, Langmuir 29 (2013) 881–891.

[27] F.-C. Wang, F. Yang, Y.-P. Zhao, Size effect on the coalescence-induced self-propelled droplet, Appl. Phys. Lett. 98 (2011), 053112.

[28] H. Cha, C. Xu, J. Sotelo, J.M. Chun, Y. Yokoyama, R. Enright, N. Miljkovic, Coalescence-induced nanodroplet jumping, Phys. Rev. Fluids 1 (2016), 064102.

[29] Y. Cheng, J. Xu, Y. Sui, Numerical investigation of coalescence-induced droplet jumping on superhydrophobic surfaces for efficient dropwise condensation heat transfer, Int. J. Heat. Mass Transf. 95 (2016) 506–516.

[30] M.D. Mulroe, B.R. Srijanto, S.F. Ahmadi, C.P. Collier, J.B. Boreyko, Tuning superhydrophobic nanostructures to enhance jumping-droplet condensation, ACS Nano 11 (2017) 8499–8510.

[31] S. Gao, Q. Liao, W. Liu, Z. Liu, Coalescence-induced jumping of nanodroplets on textured surfaces, J. Phys. Chem. Lett. 9 (2018) 13–18.

[32] J.-J. Huang, H. Huang, J.-J. Xu, Energy-based modeling of micro- and nano-droplet jumping upon coalescence on superhydrophobic surfaces, Appl. Phys. Lett. 115 (2019), 141602.

[33] F. Liu, G. Ghigliotti, J.J. Feng, C.-H. Chen, Numerical simulations of self-propelled jumping upon drop coalescence on non-wetting surfaces, J. Fluid Mech. 752 (2014) 39–65.

[34] F.-F. Xie, G. Lu, X.-D. Wang, B.-B. Wang, Coalescence-induced jumping of two unequal-sized nanodroplets, Langmuir 34 (2018) 2734–2740.

[35] Z. Liang, P. Keblinski, Coalescence-induced jumping of nanoscale droplets on super-hydrophobic surfaces, Appl. Phys. Lett. 107 (2015), 143105.

[36] X. He, L. Zhao, J. Cheng, Coalescence-Induced Swift Jumping of Nanodroplets on Curved Surfaces, Langmuir 35 (2019) 9979–9987.

[37] S. Perumanath, M.K. Borg, J.E. Sprittles, R. Enright, Molecular physics of jumping nanodroplets, Nanoscale 12 (2020) 20631–20637.

[38] S. Gao, Q. Liao, W. Liu, Z. Liu, Self-removal of multiple and multisize coalescing nanodroplets on nanostructured surfaces, J. Phys. Chem. C. 122 (2018) 20521–20526.

[39] K. Zhang, Z. Li, M. Maxey, S. Chen, G.E. Karniadakis, Self-cleaning of hydrophobic rough surfaces by coalescence-induced wetting transition, Langmuir 35 (2019) 2431–2442.

[40] Y. Nam, H. Kim, S. Shin, Energy and hydrodynamic analyses of coalescence-induced jumping droplets, Appl. Phys. Lett. 103 (2013).

[41] H. Li, W. Yang, A. Aili, T. Zhang, Insights into the Impact of Surface Hydrophobicity on Droplet Coalescence and Jumping Dynamics, Langmuir 33 (2017) 8574–8581.

[42] T. Mouterde, T.-V. Nguyen, H. Takahashi, C. Clanet, I. Shimoyama, D. Quéré, How merging droplets jump off a superhydrophobic surface: Measurements and model, Phys. Rev. Fluids 2 (2017), 112001.

[43] C. Lv, P. Hao, Z. Yao, Y. Song, X. Zhang, F. He, Condensation and jumping relay of droplets on lotus leaf, Appl. Phys. Lett. 103 (2013), 021601.

[44] Q. Yuan, X. Huang, Y.-P. Zhao, Dynamic spreading on pillar-arrayed surfaces: Viscous resistance versus molecular friction, Phys. Fluids 26 (2014), 092104.

[45] A. Vandadi, L. Zhao, J. Cheng, Resistant energy analysis of self-pulling process during dropwise condensation on superhydrophobic surfaces, Nanoscale Adv. 1 (2019) 1136–1147.

[46] S. Gao, J. Qu, Z. Liu, W. Liu, Nanoscale thin-film boiling processes on heterogeneous surfaces, Langmuir 38 (2022) 6352–6362.

[47] R.O. David, C. Marcolli, J. Fahrni, Y. Qiu, Y.A. Perez Sirkin, V. Molinero, F. Mahrt, D. Bruhwiler, U. Lohmann, Z.A. Kanji, Pore condensation and freezing is responsible for ice formation below water saturation for porous particles, Proc. Natl. Acad. Sci. U. S. A. 116 (2019) 8184–8189.

[48] D. Niu, H. Gao, G. Tang, Y. Yan, Droplet nucleation and growth in the presence of noncondensable gas: a molecular dynamics study, Langmuir 37 (2021) 9009–9016.

[49] S.-W. Chiu, H.L. Scott, E. Jakobsson, A coarse-grained model based on Morse potential for water and n-alkanes, J. Chem. Theory Comput. 6 (2010) 851–863.

[50] L. Guo, G.H. Tang, S. Kumar, Dynamic Wettability on the Lubricant-Impregnated Surface: From Nucleation to Growth and Coalescence, ACS Appl. Mater. Interfaces 12 (2020) 26555–26565.

[51] X. Ma, J. Lei, J. Xu, Line Tension of Nanodroplets on a Concave Surface, Langmuir 37 (2021) 4432–4440.

[52] E.L. Granados-Bazan, S.E. Quinones-Cisneros, U.K. Deiters, Structure and Contact Angle in Sessile Droplets of Binary Mixtures of Lennard-Jones Chains: A Molecular Dynamics Study, Langmuir 37 (2021) 10945–10957.

[53] S. Plimpton, Fast parallel algorithms for short-range molecular dynamics, J. Comput. Phys. 117 (1995) 1–19.

[54] V.I. Kalikmanov, Classical nucleation theory. Nucleation Theory, Springer,, Dordrecht, 2013, pp. 17–41.

[55] Y. Jin, A. Qamar, Y. Shi, P. Wang, Preferential water condensation on superhydrophobic nano-cones array, Appl. Phys. Lett. 113 (2018), 211601.

[56] B. Du, Y. Cheng, S. Yang, W. Xu, Z. Lan, R. Wen, X. Ma, Preferential Vapor Nucleation on Hierarchical Tapered Nanowire Bunches, Langmuir 37 (2021) 774–784.

[57] M. He, Y. Ding, J. Chen, Y. Song, Spontaneous uphill movement and self-removal of condensates on hierarchical tower-like arrays, ACS Nano 10 (2016) 9456–9462.

[58] X. Yan, Y. Qin, F. Chen, G. Zhao, S. Sett, M.J. Hoque, K.F. Rabbi, X. Zhang, Z. Wang, L. Li, F. Chen, J. Feng, N. Miljkovic, Laplace pressure driven single-droplet jumping on structured surfaces, ACS Nano 14 (2020) 12796–12809.

[59] F. Chu, X. Yan, N. Miljkovic, How superhydrophobic grooves drive single-droplet jumping, Langmuir 38 (2022) 4452–4460.

[60] Q. Peng, X. Yan, J. Li, L. Li, H. Cha, Y. Ding, C. Dang, L. Jia, N. Miljkovic, Breaking droplet jumping energy conversion limits with superhydrophobic microgrooves, Langmuir 36 (2020) 9510–9522.

[61] L. Stendardo, A. Milionis, G. Kokkoris, C. Stamatopoulos, C.S. Sharma, R. Kumar, M. Donati, D. Poulikakos, Out-of-plane biphilic surface structuring for enhanced capillary-driven dropwise condensation, Langmuir 39 (2023) 1585–1592.

[62] C. Lv, P. Hao, X. Zhang, F. He, Dewetting transitions of dropwise condensation on nanotexture-enhanced superhydrophobic surfaces, ACS Nano 9 (2015) 12311–12319.

[63] C.S. Sharma, J. Combe, M. Giger, T. Emmerich, D. Poulikakos, Growth Rates and Spontaneous Navigation of Condensate Droplets Through Randomly Structured Textures, ACS Nano 11 (2017) 1673–1682.

[64] C.S. Sharma, C. Stamatopoulos, R. Suter, P.R. von Rohr, D. Poulikakos, Rationally 3D-textured copper surfaces for laplace pressure imbalance-induced enhancement in dropwise condensation, ACS Appl. Mater. Interfaces 10 (2018) 29127–29135.

[65] S. Gao, J. Long, W. Liu, Z. Liu, Evaporation-induced wetting transition of nanodroplets on nanopatterned surfaces with concentric rings: Surface geometry and wettability effects, Langmuir 35 (2019) 9546–9553.

[66] X. Chen, R. Ma, J. Li, C. Hao, W. Guo, B.L. Luk, S.C. Li, S. Yao, Z. Wang, Evaporation of droplets on superhydrophobic surfaces: Surface roughness and small droplet size effects, Phys. Rev. Lett. 109 (2012), 116101.

[67] J.D. Paulsen, Approach and coalescence of liquid drops in air, Phys. Rev. E 88 (2013), 063010.

[68] J.D. Paulsen, J.C. Burton, S.R. Nagel, S. Appathurai, M.T. Harris, O.A. Basaran, The inexorable resistance of inertia determines the initial regime of drop coalescence, Proc. Natl. Acad. Sci. USA 109 (2012) 6857–6861.

[69] G. Li, M.H. Alhosani, S. Yuan, H. Liu, A.A. Ghaferi, T. Zhang, Microscopic droplet formation and energy transport analysis of condensation on scalable superhydrophobic nanostructured copper oxide surfaces, Langmuir 30 (2014) 14498–14511.

[70] B. Li, F. Xin, W. Tan, G. Zhu, A new theoretical model for coalescence-induced droplet jumping on hydrophobic fibers, Ind. Eng. Chem. Res. 57 (2018) 8299–8307.

[71] Y. Cheng, B. Du, K. Wang, Y. Chen, Z. Lan, Z. Wang, X. Ma, Macrotextures-induced jumping relay of condensate droplets, Appl. Phys. Lett. 114 (2019), 093704.

[72] J.-J. Huang, H. Huang, J.-J. Xu, Energy-based modeling of micro-and nano-droplet jumping upon coalescence on superhydrophobic surfaces, Appl. Phys. Lett. 115 (2019), 141602.

[73] X. Chen, R.S. Patel, J.A. Weibel, S.V. Garimella, Coalescence-induced jumping of multiple condensate droplets on hierarchical superhydrophobic surfaces, Sci. Rep. 6 (2016) 1–11.

[74] T.D. Blake, The physics of moving wetting lines, J. Colloid Interf. Sci. 299 (2006) 1–13.

[75] P. Johansson, B. Hess, Molecular origin of contact line friction in dynamic wetting, Phys. Rev. Fluids 3 (2018).

[76] R. Bey, B. Coasne, C. Picard, Carbon dioxide as a line active agent: Its impact on line tension and nucleation rate, Proc. Natl. Acad. Sci. USA 118 (2021), e2102449118.

[77] F. Staniscia, M. Kanduc, Apparent line tension induced by surface-active impurities, J. Chem. Phys. 157 (2022), 184707.

[78] B. Zhao, S. Luo, E. Bonaccurso, G.K. Auernhammer, X. Deng, Z. Li, L. Chen, Resolving the Apparent Line Tension of Sessile Droplets and Understanding its Sign Change at a Critical Wetting Angle, Phys. Rev. Lett. 123 (2019), 094501.

[79] E. Olçeroğlu, M. McCarthy, Self-organization of microscale condensate for delayed flooding of nanostructured superhydrophobic surfaces, ACS Appl. Mater. Interfaces 8 (2016) 5729–5736.

[80] N. Miljkovic, R. Enright, E.N. Wang, Modeling and optimization of superhydrophobic condensation, J. Heat. Transf. 135 (2013), 111004.

Shan Gao received his B.S. and Ph. D. degrees from Huazhong University of Science and Technology, in 2015 and 2020, respectively. He joined the School of Energy and Power Engineering in Jiangsu University as a lecturer in 2021, and currently is a postdoctoral fellow at Tsinghua University. His researches mainly focus on micro-nanostructured super-hydrophobic surfaces, micro-nanoscale liquid-vapor phase-change heat transfer, fluid dynamics and multiscale simulations.

Jian Qu is currently a professor at the School of Energy and Power Engineering in Jiangsu University. He received his Ph.D. degree in Engineering Thermophysics from Shanghai Jiao Tong University in 2010. His current research mainly focuses on micro/nanoscale fluid flow and phase-change heat transfer, interfaces and surfaces, high-power density electronic/opto-electronic cooling, and hydrogen energy storage and transportation.

Zhichun Liu is a professor in the School of Energy and Power Engineering, Huazhong University of Science and Technology of China (HUST). He received his Ph.D. from HUST in 2006, and was visiting scholar in Massachusetts Institute of Technology, US in 2012. His research focuses on heat transfer in nanoscale, electronic cooling, porous media and energy conservation. He has published more than 100 academic papers included in SCI.

Weigang Ma received the B.E. (2006) and Ph. D (2012) degrees from Tsinghua University.He is an Associate Professor (tenured), Department of Mechanical Engineering, Tsinghua University, China. His current interests mainly focus on micro/nanoscale transport and energy conversion.